RSC Advances

PAPER

View Article Online
View Journal | View Issue

Cite this: *RSC Adv.*, 2023, **13**, 18323

Thermoelectric properties of $X_3N_2O_2$ (X = Hf, Zr) MXene monolayers: a first-principles study

Xinxin Yan,[a] Wei Cao *[b] and Haohuan Li *[a]

MXene monolayers have received increasing attention due to their unique properties, particularly their high conductivity, which shows great potential in thermoelectric materials. In this paper, we present a theoretical study of the thermoelectric properties of $X_3N_2O_2$ (X = Hf, Zr) MXene monolayers, taking electron–phonon coupling into consideration. Owing to their similar geometrical structures, electronic band structures, and phonon dispersions, $X_3N_2O_2$ MXene monolayers exhibit homogeneous electron and phonon transport properties. The conduction band shows multi-valley characteristics which leads to better n-type electron transport properties than p-type ones. The maximum values of the n-type power factor can reach 32 μW cm^{-1} K^{-2} for the $Hf_3N_2O_2$ monolayer and 23 μW cm^{-1} K^{-2} for the $Zr_3N_2O_2$ monolayer. In terms of phonon transport, the lattice thermal conductivity for the $Zr_3N_2O_2$ monolayer is higher than that for the $Hf_3N_2O_2$ monolayer, due to larger phonon group velocity. Our results show that the $Hf_3N_2O_2$ monolayer is more suitable for thermoelectric materials than the $Zr_3N_2O_2$ monolayer, with optimal n-type thermoelectric figure of merit (*ZT*) values of 0.36 and 0.15 at 700 K, respectively. These findings may be useful for the development of wearable thermoelectric devices and sensor applications based on $X_3N_2O_2$ MXene monolayers.

Received 29th April 2023
Accepted 5th June 2023

DOI: 10.1039/d3ra02835f

rsc.li/rsc-advances

1 Introduction

Two-dimensional (2D) materials are extensively researched due to their unique properties, such as high surface area,[1] high conductivity,[2] and tunable band gaps,[3] which differ from their bulk counterparts. These properties make them promising materials for a wide range of applications, including electronics,[4] energy storage,[5] catalysis,[6] and sensors.[7] Furthermore, 2D materials can be easily integrated with other materials, making them a versatile platform for developing new technologies. Researchers continue to explore the potential of 2D materials and their applications, leading to exciting new discoveries and advancements in various fields. MXenes are a family of 2D transition metal carbides, nitrides, and carbonitrides. They were first discovered in 2011.[8] The general formula for MXenes is $M_{n+1}X_nT_x$, where M is a transition metal, X is carbon or nitrogen, and *T* is a surface termination such as O, OH, F, and/or Cl.[9] The structure of an MXene monolayer consists of layers of transition metal atoms stacked on top of each other, with the X and T atoms occupying the interstitial sites between them. The transition metal atoms are connected by covalent bonds, while the X and T atoms are connected to the transition metal atoms by ionic bonds. The MXene monolayer can be viewed as a sandwich structure, where the transition metal atoms form the bread and the X and T atoms form the filling. The sandwich structure can be peeled off layer by layer to produce MXene flakes, which have a thickness of a few nanometers.[10] MXene monolayers usually possess high electrical conductivity,[11] efficient absorption of electromagnetic waves,[12] and tunable mechanical properties.[13] Modifying the functionalized surfaces can be an effective way to modulate the properties of MXene monolayers.[14] These unique properties make MXenes promising materials for a variety of applications.[15–17]

Thermoelectric materials are a special type of material that can convert temperature differences into electrical energy and *vice versa*.[18] The efficiency of a thermoelectric material is measured by its thermoelectric figure of merit, *ZT*.[19] The higher the *ZT* value of a material, the more efficient it is in converting temperature differences into electrical energy. The thermoelectric figure of merit, *ZT*, is defined by the equation: $ZT = S^2\sigma T/(\kappa_l + \kappa_e)$, where *S* is the Seebeck coefficient, σ is the electrical conductivity, *T* is the absolute temperature, and κ_l and κ_e are the lattice and electronic thermal conductivity, respectively. As mentioned previously, the high conductivity of MXenes makes them promising applications for thermoelectric materials. There have already been many studies on the thermoelectric properties of MXenes. For example, Kumar *et al.*[20] investigated the electronic and thermal properties of different functionalizations in the Sc_2C MXenes. They found that $Sc_2C(OH)_2$ possesses high electrical conductivity and relatively low lattice thermal conductivity, indicating it is a candidate for

[a]*Department of Orthopedics, Renmin Hospital, Wuhan University, Wuhan 430060, China. E-mail: lihaohuan@whu.edu.cn*

[b]*The Institute of Technological Sciences, Wuhan University, Wuhan 430072, China. E-mail: wei_cao@whu.edu.cn*

intermediate-temperature thermoelectric. Meanwhile, the role of functionalized surfaces on thermoelectric properties in M_2C and M_2N MXenes was also studied.[21] The results showed that Mo_2C can gain a large Seebeck coefficient. Flexible film electrodes have been designed using a ternary composite of $Ti_3C_2T_x$ MXene.[22] Recently, Rana *et al.* investigated the narrow bandgap Janus monolayer $MoWCO_2$.[23] The thermoelectric figure of merit was 0.33 (p-type) and 0.08 (n-type) at 700 K. Experimental work was also carried out, and the power factor (PF) of $Mo_2TiC_2T_x$ film can reach 309 μW cm^{-1} K^{-2} at 800 K.[24]

However, the thermoelectric properties of the $X_3N_2O_2$ MXene monolayer have not been studied yet. In this paper, we calculate these properties for $X_3N_2O_2$ (X = Hf, Zr) using first principles and Boltzmann transport theory, including electron–phonon coupling. Our work provides a full understanding of the electron–phonon coupling on MXene monolayers with high accuracy, and can be expanded to the study of more thermoelectric materials.

2 Computational methods

All first-principles calculations were performed using density functional theory (DFT), as implemented in the Quantum ESPRESSO (QE) code.[25,26] The exchange-correlated interactions were described using the generalized gradient approximation of the Perdew–Burke–Ernzerhof (GGA-PBE).[27] The corresponding pseudopotential files were obtained from the Standard solid-state pseudopotentials (SSSP) libraries.[28] The wave function was expanded using a plane-wave cutoff energy of 80 Ry. The Brillouin zone was sampled using an 11 × 11 × 1 *k*-point mesh according to the Monkhorst–Pack scheme.[29] A vacuum slab of 15 Å was applied along the *c*-direction. The energy and force convergence thresholds were set to 10^{-10} Ry and 10^{-4} Ry, respectively, in order to fully relax the structure.

Electrical transport coefficients were calculated using Boltzmann transport theory as implemented in the BoltzTraP code.[30] Under the electron–phonon averaged (EPA) approximation,[31] the carrier relaxation time (τ_e) was evaluated using the following equation:

$$\tau_e^{-1}(\varepsilon,\mu,T) = \frac{2\pi\Omega}{g_s\hbar}\sum_{\nu}\{g_\nu{}^2(\varepsilon,\varepsilon+\overline{\omega}_\nu)[n(\overline{\omega}_\nu,T)+f(\varepsilon+\overline{\omega}_\nu,\mu,T)] \times \rho(\varepsilon+\overline{\omega}_\nu) + g_\nu{}^2(\varepsilon,\varepsilon-\overline{\omega}_\nu) [n(\overline{\omega}_\nu,T)+1-f(\varepsilon-\overline{\omega}_\nu,\mu,T)]\rho(\varepsilon-\overline{\omega}_\nu)\} \quad (1)$$

Here, ε is the energy of the carriers, μ is the chemical potential, Ω is the volume of the primitive unit cell, $\hbar$ is the reduced Planck's constant, g_s is the spin degeneracy, ν is the phonon mode index, $g_\nu{}^2$ is the averaged electron–phonon matrix, $\bar{\omega}\times\nu$ is the averaged phonon mode energy, $n(\bar{\omega}\times\nu, T)$ is the Bose–Einstein distribution function, $f(\varepsilon+\bar{\omega}\nu, \mu, T)$ is the Fermi–Dirac distribution function, and ρ is the density of states per unit energy and unit volume. Details about this method can be found in the ref. 31.

The value of κ_l is obtained by solving phonon Boltzmann transport theory, as implemented in the ShengBTE code.[32] The second-order harmonic interatomic force constants (IFCs) were calculated by density functional perturbation theory (DFPT) using a supercell of 5 × 5 × 1. The third-order anharmonic IFCs were calculated using the finite displacement method with the same supercell. To obtain a convergent κ_l, a cutoff distance of up to the 9th nearest atomic neighbors was used. The *q*-point grid was set to 60 × 60 × 1, and the smearing parameter was set to 1.0.

3 Results and discussion

The geometrical structures of $Hf_3N_2O_2$ and $Zr_3N_2O_2$ monolayers are illustrated in Fig. 1(a) and (b), respectively. These monolayers possess a hexagonal crystal structure with a space group of *P*6/*mmm*. This space group has a six-fold rotational symmetry axis and mirror planes that intersect at the *c*-axis of the crystal. The optimized lattice constants of $Hf_3N_2O_2$ and $Zr_3N_2O_2$ monolayers are 3.210 Å and 3.245 Å, respectively. Their lattice constants are close, indicating that their bond strengths are similar.

Fig. 1(c) shows a comparison of the band structures of $Hf_3N_2O_2$ and $Zr_3N_2O_2$ monolayers. The bands are similar, with the conduction band minimum (CBM) at the *M* point and the valence band maximum (VBM) at the *K* point. The band gap of $Hf_3N_2O_2$ and $Zr_3N_2O_2$ monolayers is 0.328 eV and 0.394 eV, respectively. The band gap of $Hf_3N_2O_2$ is smaller than that of $Zr_3N_2O_2$. Moreover, the conduction band has multiple valleys, while the valence band is relatively simple. The multiple valleys in the band result in a high density of states (DOS) and a high *S* value.

To gain a better understanding of the electronic properties of monolayers $Hf_3N_2O_2$ and $Zr_3N_2O_2$, we show their projected density of states (pDOS) in Fig. 2(a) and (b), respectively. This paper ignores the projected DOS for other orbitals due to their ultralow values. The pDOS of $Hf_3N_2O_2$ is similar to that of $Zr_3N_2O_2$, with the former mainly contributed by the Hf 5d electrons and the latter mainly contributed by the Zr 4d electrons. Furthermore, the DOS of $Zr_3N_2O_2$ is higher than that of $Hf_3N_2O_2$. The multiple valleys in the conduction band can be attributed to the Hf 5d or Zr 4d electrons.

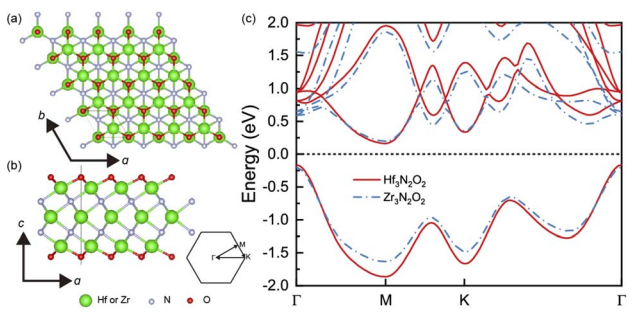

Fig. 1 The crystal structure of $Hf_3N_2O_2$ and $Zr_3N_2O_2$ monolayer on the (a) top view and (b) side view. (c) The band structure of $Hf_3N_2O_2$ and $Zr_3N_2O_2$ monolayer.

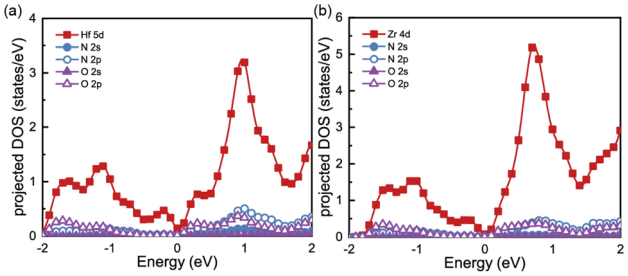

Fig. 2 The projected density of states (DOS) for (a) $Hf_3N_2O_2$ and (b) $Zr_3N_2O_2$ monolayer.

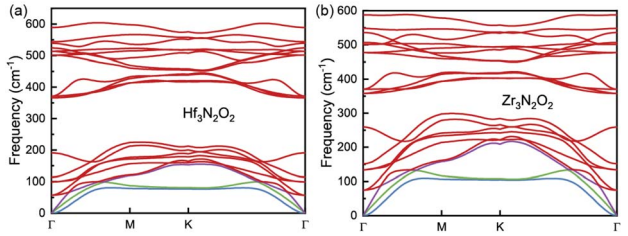

Fig. 3 The harmonic phonon dispersion for (a) $Hf_3N_2O_2$ and (b) $Zr_3N_2O_2$ monolayer.

The phonon dispersion curves of $Hf_3N_2O_2$ and $Zr_3N_2O_2$ monolayers are shown in Fig. 3(a) and (b), respectively. It can be seen that the phonon dispersion curves of both monolayers are generally similar. Both $Hf_3N_2O_2$ and $Zr_3N_2O_2$ monolayers are dynamically stable due to the absence of imaginary modes. There is a clear band gap around 300 cm^{-1}, with $Hf_3N_2O_2$ monolayer exhibiting a wider gap than the $Zr_3N_2O_2$ monolayer. The low frequency part (< 300 cm^{-1}) of $Hf_3N_2O_2$ monolayer is lower than that of $Zr_3N_2O_2$ monolayer. The slopes of the acoustic modes (marked by another color) for $Zr_3N_2O_2$ monolayer are larger than those of $Hf_3N_2O_2$ monolayer. This suggests that $Zr_3N_2O_2$ monolayer would exhibit larger phonon group velocity (v_g), which will be further confirmed.

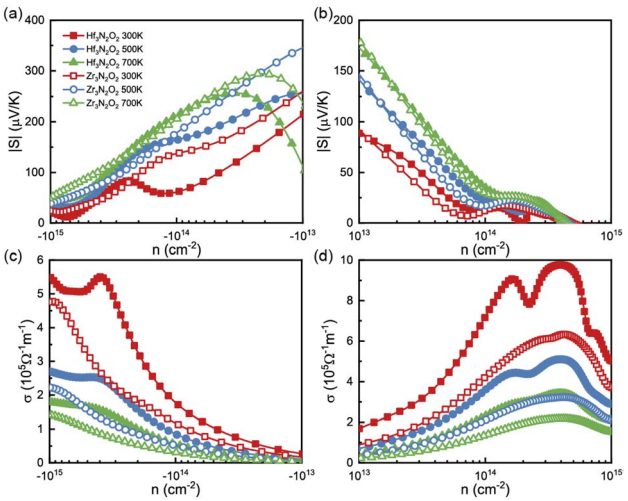

Fig. 4 The (a), (b) $|S|$ and (c), (d) σ as a function of carrier concentration for $Hf_3N_2O_2$ and $Zr_3N_2O_2$ monolayer.

To analyze the thermoelectric transport properties, we first illustrate the absolute values of Seebeck coefficient ($|S|$) in Fig. 4(a) and (b). S can be attribute to the steep slope of the DOS,[33] *i.e.*, $\partial n(\varepsilon)/\partial\varepsilon$. Owing the DOS peak in conduction caused by Hf 5d or Zr 4d electrons, the absolute values of n-type S are much higher than p-type ones. We fit the steep slope of the DOS between 0.2–0.7 eV, which corresponds to a moderate n-type carrier concentration. The fitted steep slopes of the DOS are 6.55 and 10.47 for $Hf_3N_2O_2$ and $Zr_3N_2O_2$, respectively. These values are consistent with the n-type $|S|$ (62 and 138 μV K^{-1} for $Hf_3N_2O_2$ and $Zr_3N_2O_2$, respectively) at 300 K. At a moderate concentration (10^{-14} cm^{-2}), n-type $|S|$ can reach 200 μV K^{-1} at 700 K, while p-type $|S|$ is only 30 μV K^{-1}. The high n-type S implies that $Zr_3N_2O_2$ monolayers are potential n-type thermoelectric materials. Additionally, the absolute values of p-type S are higher than those of n-type S.

Since σ and κ_e are dependent on electronic relaxation time (τ_e), we need to analyze τ_e first. Fig. 5(a) and (b) show τ_e as a function of energy at various temperatures. Unlike the constant relaxation time approximation method and deformation potential theory, τ_e calculated by EPA depends firmly on the carrier density, which is more accurate. As energy approaches the Fermi level, τ_e increases. All $X_3N_2O_2$ monolayers have much higher τ_e for holes than for electrons. We attribute this phenomenon to the more dispersive valence band than the conduction band. There are many conduction band valleys near the Fermi level, which scatter charge carriers more easily and lead to a lower τ_e for electrons. As temperature increases, charge carrier scattering becomes stronger and a lower τ_e is observed at higher temperatures.

Fig. 4(c) and (d) plot σ as a function of energy at different temperatures, based on τ_e. Contrary to S, the σ of n-type doping are much lower than that of their p-type doping. For a moderate concentration (10^{-14} cm^{-2}), p-type σ for $Hf_3N_2O_2$ monolayer can exceed 7 × 10^5 Ω^{-1} m^{-1} at room temperature. As expected, σ increases for increasing higher carrier concentration. As temperature increases, σ decreases due to stronger carrier scattering, which is the same as τ. According to the Wiedemann–Franz law, κ_e is proportional to σ: $\kappa_e = L\sigma T$, where L is the Lorenz number.[34] Therefore, there is no need to analyze κ_e separately.

By combining the results of S and σ, we can determine the power factor (PF) of monolayers of $X_3N_2O_2$, as shown in Fig. 6(a) and (b). The PF of the $Hf_3N_2O_2$ monolayer is higher than that of the $Zr_3N_2O_2$ monolayer. Additionally, the p-type PF is much

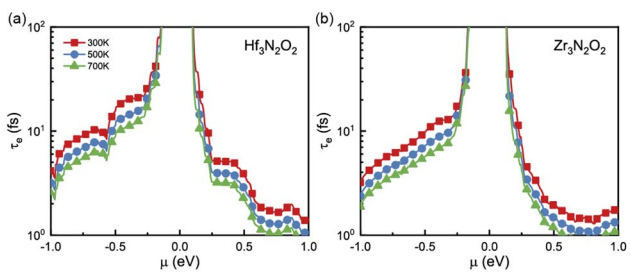

Fig. 5 The electronic relaxation time (τ_e) of (a) $Hf_3N_2O_2$ and (b) $Zr_3N_2O_2$ monolayers as a function of the energy.

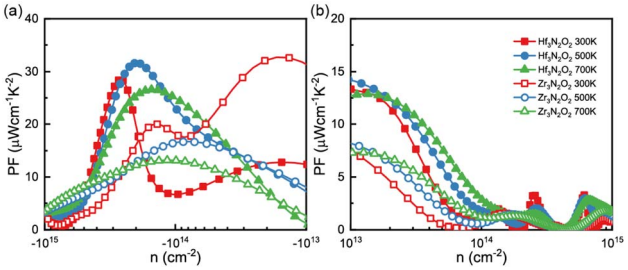

Fig. 6 The (a) n-type nad (b) p-type power factor (PF) values as a function of carrier concentration for $Hf_3N_2O_2$ and $Zr_3N_2O_2$ monolayer.

lower than the n-type PF, indicating that $X_3N_2O_2$ monolayers are more suited for n-type thermoelectric materials. Interestingly, the PF of the $Zr_3N_2O_2$ monolayer reaches its maximum value at 300 K (23 μW cm^{-1} K^{-2}) and decreases with temperature, while the PF of the $Hf_3N_2O_2$ monolayer is weakly temperature-dependent. The n-type maximum PF values for $Hf_3N_2O_2$ can reach 32 μW cm^{-1} K^{-2} at 500 K. For both materials, the maximum p-type PF values are half that of n-type.

The phononic transport properties of $X_3N_2O_2$ monolayers, including κ_l, Gruneisen parameter, phonon group velocity, and phonon relaxation time, are shown in Fig. 7(a)–(d). At room temperature, κ_l for $Hf_3N_2O_2$ and $Zr_3N_2O_2$ monolayer is 14.5 and 16 W mK^{-1}, respectively. As with other crystalline materials, κ_l decreases as temperature increases, following a $1/T$ dependence. Higher temperature causes intrinsic enhancement in phonon–phonon scattering. With temperature increasing to 700 K, κ_l for $Hf_3N_2O_2$ and $Zr_3N_2O_2$ monolayer decreases to 5.55 and 6.18 W mK^{-1} which is relatively acceptable for thermoelectric applications.

It can be noticed that κ_l for $Hf_3N_2O_2$ monolayer is always lower than that of $Zr_3N_2O_2$ monolayer. κ_l is determined mainly by phonon group velocity (v_g) and phonon relaxation time (τ_{ph}), as $\kappa_l \propto v_g\tau_{ph}$. The v_g for $Zr_3N_2O_2$ monolayer is higher than that of $Hf_3N_2O_2$ monolayer for low frequency part (<300 cm^{-1}) as

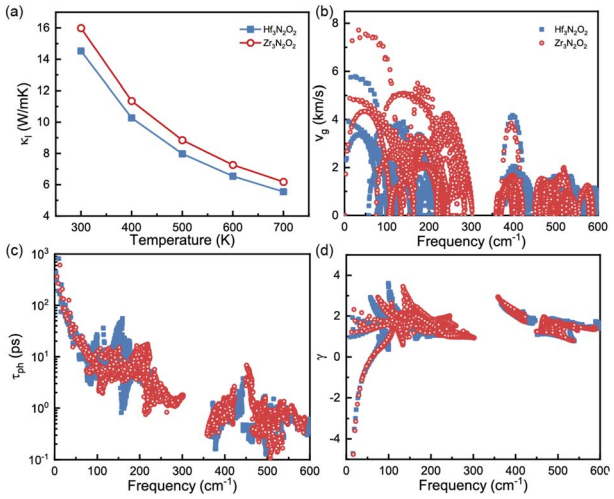

Fig. 7 (a) κ_l, (b) phonon group velocity, (c) phonon lifetime, and (d) Gruneisen parameter for $Hf_3N_2O_2$ and $Zr_3N_2O_2$ monolayer.

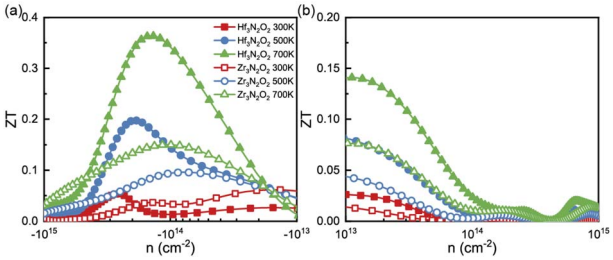

Fig. 8 The (a) n-type and (b) p-type ZT values as a function of carrier concentration for $Hf_3N_2O_2$ and $Zr_3N_2O_2$ monolayer.

shown in Fig. 7(b). The v_g at Γ point can reach 8 km s^{-1} for $Zr_3N_2O_2$ monolayer, while the corresponding v_g of $Hf_3N_2O_2$ monolayer is 6 km s^{-1}. For high frequency part (>300 cm^{-1}), v_g for $X_3N_2O_2$ monolayers are similar. This can be confirmed by the phonon dispersion curves in Fig. 3, as $v_g = \partial\omega_{\lambda,q}/\partial q$. Different from v_g, τ_{ph} for $X_3N_2O_2$ monolayers are close, as plotted in Fig. 7(c). Especially for low frequency (<50 cm^{-1}), τ_{ph} for $X_3N_2O_2$ monolayers are nearly the same. We further analyze the Gruneisen parameter (γ). γ reflects the anharmonic scattering strength[35] which is given by $\gamma = -(V/\omega_{\lambda,q})\partial\omega_{\lambda,q}/\partial V$. Larger $|\gamma|$ means stronger anharmonicity and phonon–phonon scattering. Obviously, γ for $X_3N_2O_2$ monolayers are basically the same, as shown in Fig. 7(d). The difference in v_g caused by phonon dispersions is the main reason for lower κ_l of $Hf_3N_2O_2$ monolayer than $Zr_3N_2O_2$ monolayer, while τ_{ph} and anharmonic scattering strength for $X_3N_2O_2$ monolayers are similar.

Combining with calculated PF and κ_l, we calculated the ZT values as a function of n as plotted in Fig. 8(a) and (b). $X_3N_2O_2$ monolayers exhibit higher n-type ZT values than p-type ones. Additionally, the ZT values of $Hf_3N_2O_2$ monolayer are higher than those of $Zr_3N_2O_2$ monolayer. For n-type $Hf_3N_2O_2$ monolayer, ZT values present an behavior of monotonically increasing with temperature and optimal n gradually move to the low concentration. More specifically, maximum ZT values can reach 0.36 at 700 K. For p-type $Hf_3N_2O_2$ monolayer, ZT values are relatively low and the optimal n is around 10^{20} cm^{-3}. The maximum ZT value for n-type $Zr_3N_2O_2$ monolayer is 0.15 at 700 K. Although all $X_3N_2O_2$ monolayers exhibit high power factors (PF), their final ZT values are relatively low due to their high κ_l. Future work should focus on reducing κ_l to improve the ZT values. For example, alloying with other elements to reduce the phonon group velocity and/or increasing the phonon scattering strength by introducing defects or nanostructures.

4 Conclusions

In this paper, we studied the thermoelectric properties of the $X_3N_2O_2$ (X = Hf, Zr) MXene monolayers using first-principles calculations and Boltzmann transport theory. To obtain accurate electrical transport properties, we took electron–phonon coupling into consideration. We found that $Hf_3N_2O_2$ and $Zr_3N_2O_2$ monolayers have similar structures, band structures, and phonon dispersions. The narrow band gap (0.3 eV) ensures high electrical conductivity. The $Hf_3N_2O_2$ monolayer exhibits a better power factor and lower lattice thermal conductivity than

the $Zr_3N_2O_2$ monolayer. The maximum *ZT* value achieved for n-type $Hf_3N_2O_2$ monolayer at 700 K is 0.36.

Author contributions

X. Y. and W. C. conceived the study. W. C. performed the calculations and analyzed the data. X. Y. and H. L. wrote, reviewed, and edited the manuscript. All authors have read and agreed to the published version of the manuscript.

Conflicts of interest

There are no conflicts to declare.

Acknowledgements

This research was funded by the Fundamental Research Funds for the Central Universities: 2042022kf1078 and the Knowledge Innovation Program of Wuhan-Basic Research (No. 2022020801010473).

References

1 C. Anichini, W. Czepa, D. Pakulski, A. Aliprandi, A. Ciesielski and P. Samorì, *Chem. Soc. Rev.*, 2018, **47**, 4860–4908.
2 F. Wu, H. Tian, Y. Shen, Z.-Q. Zhu, Y. Liu, T. Hirtz, R. Wu, G. Gou, Y. Qiao, Y. Yang, C.-Y. Xing, G. Zhang and T.-L. Ren, *Adv. Mater. Interfaces*, 2022, **9**, 2200409.
3 X. Bao, Q. Ou, Z.-Q. Xu, Y. Zhang, Q. Bao and H. Zhang, *Adv. Mater. Technol.*, 2018, **3**, 1800072.
4 Y. Pang, Z. Yang, Y. Yang and T.-L. Ren, *Small*, 2020, **16**, 1901124.
5 L. Lin, J. Chen, D. Liu, X. Li, G. G. Wallace and S. Zhang, *Adv. Energy Mater.*, 2020, **10**, 2002621.
6 F. R. Fan, R. Wang, H. Zhang and W. Wu, *Chem. Soc. Rev.*, 2021, **50**, 10983–11031.
7 L. Zhang, K. Khan, J. Zou, H. Zhang and Y. Li, *Adv. Mater. Interfaces*, 2019, **6**, 1901329.
8 M. Naguib, M. Kurtoglu, V. Presser, J. Lu, J. Niu, M. Heon, L. Hultman, Y. Gogotsi and M. W. Barsoum, *Adv. Mater.*, 2011, **23**, 4248–4253.
9 B. Anasori, M. R. Lukatskaya and Y. Gogotsi, *Nat. Rev. Mater.*, 2017, **2**, 16098.
10 Y. Gogotsi and B. Anasori, *ACS Nano*, 2019, **13**, 8491–8494.
11 D. H. Ho, Y. Y. Choi, S. B. Jo, J.-M. Myoung and J. H. Cho, *Adv. Mater.*, 2021, **33**, 2005846.
12 C. Cui, R. Guo, E. Ren, H. Xiao, M. Zhou, X. Lai, Q. Qin, S. Jiang and W. Qin, *Chem. Eng. J.*, 2021, **405**, 126626.
13 B. C. Wyatt, A. Rosenkranz and B. Anasori, *Adv. Mater.*, 2021, **33**, 2007973.
14 X.-H. Zha, K. Luo, Q. Li, Q. Huang, J. He, X. Wen and S. Du, *Europhys. Lett.*, 2015, **111**, 26007.
15 Y. Liu, J. Yu, D. Guo, Z. Li and Y. Su, *J. Alloys Compd.*, 2020, **815**, 152403.
16 M. Seredych, C. E. Shuck, D. Pinto, M. Alhabeb, E. Precetti, G. Deysher, B. Anasori, N. Kurra and Y. Gogotsi, *Chem. Mater.*, 2019, **31**, 3324–3332.
17 M. Zohair, K. Moyer, J. Eaves-Rathert, C. Meng, J. Waugh and C. L. Pint, *ACS Nano*, 2020, **14**, 2308–2315.
18 N. Jia, J. Cao, X. Y. Tan, J. Dong, H. Liu, C. K. I. Tan, J. Xu, Q. Yan, X. J. Loh and A. Suwardi, *Mater. Today Phys.*, 2021, **21**, 100519.
19 G. J. Snyder and E. S. Toberer, *Nat. Mater.*, 2008, **7**, 105–114.
20 S. Kumar and U. Schwingenschlögl, *Phys. Rev. B*, 2016, **94**, 035405.
21 M. Khazaei, M. Arai, T. Sasaki, M. Estili and Y. Sakka, *Phys. Chem. Chem. Phys.*, 2014, **16**, 7841–7849.
22 S. Wei, J. Ma, D. Wu, B. Chen, C. Du, L. Liang, Y. Huang, Z. Li, F. Rao, G. Chen and Z. Liu, *Adv. Funct. Mater.*, 2023, **33**, 2209806.
23 G. Rana, R. Gupta and C. Bera, *Appl. Phys. Lett.*, 2023, **122**, 063902.
24 H. Kim, B. Anasori, Y. Gogotsi and H. N. Alshareef, *Chem. Mater.*, 2017, **29**, 6472–6479.
25 P. Giannozzi, S. Baroni, N. Bonini, M. Calandra, R. Car, C. Cavazzoni, D. Ceresoli, G. L. Chiarotti, M. Cococcioni, I. Dabo, A. D. Corso, S. de Gironcoli, S. Fabris, G. Fratesi, R. Gebauer, U. Gerstmann, C. Gougoussis, A. Kokalj, M. Lazzeri, L. Martin-Samos, N. Marzari, F. Mauri, R. Mazzarello, S. Paolini, A. Pasquarello, L. Paulatto, C. Sbraccia, S. Scandolo, G. Sclauzero, A. P. Seitsonen, A. Smogunov, P. Umari and R. M. Wentzcovitch, *J. Phys.: Condens. Matter*, 2009, **21**, 395502.
26 P. Giannozzi, O. Andreussi, T. Brumme, O. Bunau, M. B. Nardelli, M. Calandra, R. Car, C. Cavazzoni, D. Ceresoli, M. Cococcioni, N. Colonna, I. Carnimeo, A. D. Corso, S. de Gironcoli, P. Delugas, R. A. DiStasio, A. Ferretti, A. Floris, G. Fratesi, G. Fugallo, R. Gebauer, U. Gerstmann, F. Giustino, T. Gorni, J. Jia, M. Kawamura, H.-Y. Ko, A. Kokalj, E. Küçükbenli, M. Lazzeri, M. Marsili, N. Marzari, F. Mauri, N. L. Nguyen, H.-V. Nguyen, A. O. de-la Roza, L. Paulatto, S. Poncé, D. Rocca, R. Sabatini, B. Santra, M. Schlipf, A. P. Seitsonen, A. Smogunov, I. Timrov, T. Thonhauser, P. Umari, N. Vast, X. Wu and S. Baroni, *J. Phys.: Condens. Matter*, 2017, **29**, 465901.
27 J. P. Perdew, K. Burke and M. Ernzerhof, *Phys. Rev. Lett.*, 1996, **77**, 3865–3868.
28 G. Prandini, A. Marrazzo, I. E. Castelli, N. Mounet and N. Marzari, *npj Comput. Mater.*, 2018, **4**, 72.
29 H. J. Monkhorst and J. D. Pack, *Phys. Rev. B*, 1976, **13**, 5188–5192.
30 G. K. Madsen and D. J. Singh, *Comput. Phys. Commun.*, 2006, **175**, 67–71.
31 G. Samsonidze and B. Kozinsky, *Adv. Energy Mater.*, 2018, **8**, 1800246.
32 W. Li, J. Carrete, N. A. Katcho and N. Mingo, *Comput. Phys. Commun.*, 2014, **185**, 1747–1758.
33 J. Mao, Z. Liu and Z. Ren, *npj Quantum Mater.*, 2016, **1**, 16028.
34 R. Venkatasubramanian, E. Siivola, T. Colpitts and B. O'Quinn, *Nature*, 2001, **413**, 597–602.
35 D. A. Broido, A. Ward and N. Mingo, *Phys. Rev. B*, 2005, **72**, 014308.